

Kinematics of the anemic cluster galaxy NGC 4548

Is stripping still active ?

B. Vollmer^{1,3}, V. Cayatte³, A. Boselli^{4,5}, C. Balkowski³ and W.J. Duschl^{1,2}

¹ Institut für Theoretische Astrophysik der Universität Heidelberg, Tiergartenstraße 15, D-69121 Heidelberg, Germany.

² Max-Planck-Institut für Radioastronomie, Auf dem Hügel 69, D-53121 Bonn, Germany.

³ Observatoire de Paris, DAEC, UMR 8631, CNRS et Université Paris 7, F-92195 Meudon Cedex, France.

⁴ Laboratoire d'Astronomie Spatiale du CNRS, BP 8, Traverse du Siphon, F-13376 Marseille Cedex 12, France.

⁵ Visiting Astronomer, Kitt Peak national Observatory, National Optical Astronomical Observatories.

Received / Accepted

Abstract. We present new HI (20'' resolution) and CO observations of NGC 4548, an anemic galaxy in the Virgo cluster. The atomic gas distribution shows a ring structure which is distorted at the northern edge. The overall rotation curve is derived with a tilted ring model. We compare our rotation curve with previous ones and discuss the differences. The velocity field of the CO pointings fit very well with the one of the atomic gas where they overlap. The CO emission permits to extend the rotation curve towards the galaxy centre. The molecular fraction is derived for the inner 120'' × 120'' centered on the galaxy. We compare the HI and CO emission to H α line and optical blue emission maps. The bar in the centre favors star formation at the outer end of the bar. The HI intensity distribution and velocity field of the northern perturbation are deprojected with the help of a first order kinematical model. They are discussed in the framework of warps. It is concluded that the scenario of ram pressure stripping responsible for the gas removal and the northern perturbation is a very probable one. In this case the ram pressure which may have caused the galaxy's HI deficiency is now fading after the galaxy's close passage to the cluster centre or increasing again due to a second approach of the galaxy to the cluster centre.

galaxy's properties, i.e. morphology, luminosity and gas content as they enter the cluster.

- galaxy-galaxy gravitational interactions
- galaxy-cluster gravitational interactions due to the cluster potential
- galaxy-cluster interaction due to an individual galaxy's motion in the hot plasma of the cluster (ram pressure stripping).

In the case of galaxy-galaxy interactions one can observe important distortions of the stellar and gas content (see e.g. Barnes & Hernquist 1996, Combes 1997, Moore et al. 1996, Olson & Kwan 1990) as the tidal forces act on both components of the galaxy. The influence of the cluster potential can cause distortions of the stellar and gas content and its velocity field only if the galaxy passes near enough the cluster centre (Valluri 1993). However, ram pressure stripping (Gunn & Gott 1972) is only acting on the gas content. This provides a tool to discriminate between these kinds of interactions (Combes et al. 1988).

Spiral galaxies located near the cluster centre show very different gas characteristics in a cluster than in the field. They are very deficient in HI (Chamaraux et al. 1980, Bothun et al. 1982, Giovanelli & Haynes 1985, Gavazzi 1987, 1989) and their HI disk sizes are also considerably reduced (van Gorkom & Kotanyi 1985, Warmels 1988, Cayatte et al. 1990, 1994). Concerning the stellar content, their intrinsic colour indices are not significantly different from field galaxies of the same morphological type (Gavazzi et al. 1991, Gavazzi et al. 1998). There is a special class of galaxies with a very low arm inter-arm contrast defined as anemics by van den Bergh (1976). But despite the HI deficiency, cluster galaxies do not show a reduced CO content (Kenney & Young 1986, Casoli et al. 1991, Boselli et al. 1997a) neither a reduced infrared luminosity (Bicay & Giovanelli 1987).

A promising way to study the galaxy's interaction with its environment is to look at details in the emission of the interstellar gas and its velocity distribution. As the atomic

Key words: Galaxies: individual: NGC 4548 – Galaxies: interactions – Galaxies: ISM – Galaxies: kinematics and dynamics

1. Introduction

A galaxy cluster is an ideal laboratory for studying the influence of the galaxy's environment on its appearance and/or evolution. There are three types of interaction which can provide the mechanisms for changing the

Send offprint requests to: B. Vollmer, e-mail: Bernd.Vollmer@obspm.fr

gas is located at large galactic radii and is relatively diffuse, it is the most sensible tracer for perturbations which are induced by forces exterior to the galaxy.

The most common distortion of the outer HI content of spiral galaxies in general are warps. They can be described by a collection of spinning, concentric rings whose angular momentum vector is more and more inclined with increasing radius (Rogstad et al. 1974). Thus, the un-tilted warp is a completely symmetric feature. Warps are a common feature in spiral galaxies (see e.g. Sancisi 1976, Bosma 1978, and Briggs 1990) although their origin is still not clear (see e.g. Binney 1992, Jiang & Binney 1999).

- It can be interpreted as a discrete bending mode in flattened halos (Lynden-Bell 1965, Sparke 1984, Sparke & Casertano 1988). However, if the proper dynamics of the halo are taken into account, the warp fades away rapidly (Nelson & Tremaine 1995, Binney et al. 1998).
- According to cosmology galactic halos should be disturbed (Ryden & Gunn 1987, Ryden 1988, Quinn & Binney 1991). They are not in dynamical equilibrium and could so generate a warped disc.
- Infalling galaxies could tidally induce or form a warp or a polar ring (Jiang & Binney 1999).
- Non-gravitational forces as ram pressure or magnetic pressure could be responsible for a warp.

Binney (1992) points out, that ram pressure stripping should cause an axisymmetric response which has the form of a rim.

In this paper, we present and discuss a new detailed HI map of the anemic galaxy NGC 4548 which is located at 2.4° from the centre of the Virgo cluster looking at the kinematics in detail. The HI map is compared to an H α line map and an optical B image. CO pointings with velocity information are added to the cube in order to give more informations about the kinematics at small galactic radii. A rotation curve is fitted and compared to the ones obtained by Guhathakurta et al. (1988) and Rubin et al. (1999). The local perturbation observed is discussed in the framework of warps.

2. Observations and data reduction

2.1. The HI data

The observations were made with the NRAO's Very Large Array (VLA) ¹, for description see Napier et al. (1983). The field was centered on NGC 4548 (Table 1). We observed in December 20 1994 for 235 minutes with the C configuration and in March 29 1995 for 90 minutes with the D configuration. A Hanning smoothing was applied on-line to the initial frequency channels, yielding 63

Table 1. The parameters of NGC 4548. Col. (1) and (2): 1950 celestial coordinates. Col. (3): morphological type (de Vaucouleurs et al. 1973). Col. (4): heliocentric velocity, in km s^{-1} . Col. (5): HI flux, in Jy km s^{-1} . Col. (6): HI deficiency (Cayatte et al. 1994).

$\alpha(1950)$	$\delta(1950)$	<i>type</i>	v_{hel}	HI flux	HI def
12h32m55.10s	14°46'20.0"	<i>SBB(sr)</i>	486	9.4	0.77

channels covering a total velocity width of 630 km s^{-1} . The velocity channels are centered on $v \sim 500 \text{ km s}^{-1}$. The data were calibrated using the standard VLA reduction programs (AIPS). A CLEANed image of all strong continuum sources were made and afterwards directly subtracted from the UV data cube. At the end a linear interpolation of the UV data points with respect to the frequency channels using the first and last 10 channels was made in order to subtract the continuum. The resulting image was CLEANed with a $20'' \times 20''$ FWHM beam. We ended up with a r.m.s. noise of $\sigma = 0.4 \text{ mJy/beam}$ in one 10 km s^{-1} channel, or $\sigma = 4.7 \times 10^{19} \text{ cm}^{-2}$ expressed in column density.

2.2. The CO data

NGC 4548 was observed in 1994 with the IRAM 30 m telescope at Pico Veleta (Granada, Spain). The beam size of the telescope is $22''$ at 115 GHz [$^{12}\text{CO}(J=1-0)$], which corresponds to 1.8 kpc at a distance of 17 Mpc. Weather conditions were good, with typical zenith opacities of 0.25-0.45. The pointing accuracy was checked hourly by broad band continuum observations of the nearby source 3C273; the average error was $3''$ rms. We used a SIS receiver in single sideband mode with $T_{\text{rec}} = 140-270 \text{ K}$ and $T_{\text{sys}} = 500-800 \text{ K}$ (in T_A^* scale) at the elevation of the source. Two filter banks of 512 contiguous 1MHz channels provided a velocity resolution of 2.6 km s^{-1} and a total velocity coverage of 1330 km s^{-1} . We used a wobbler switching procedure, with a wobbler throw of $4'$ in azimuth. Each 8 minute scan began by a chopper wheel calibration on a load at ambient temperature and a cold load. The total integration time on each position was between 16 and 54 minutes on+off (i.e. half time on source) depending on the intensity of the signal, yielding a rms noise level of 15-30 mK (in the T_{mb} scale) after boxcar velocity smoothing to 20.8 km s^{-1} .

NGC 4548 was observed at the nominal central coordinates and at different position offsets of $40''$ (Fig.1). The galaxy was observed in 25 different positions and detected in 23 of them in the CO(1-0) line.

The data were reduced with the CLASS package (Forveille et al. 1990). The baselines were generally flat owing to the use of the wobbler, allowing us to subtract

¹ The National Radio Astronomy Observatory is operated by Associated Universities Inc under a cooperative agreement with the National Science Foundation.

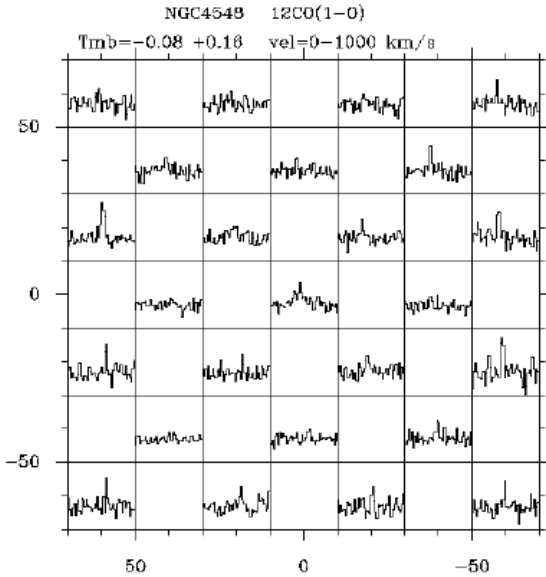


Fig. 1. The $^{12}\text{CO}(1-0)$ spectra plotted on a α - δ map centered on the nucleus of NGC 4548. The map's axes are offsets in arcseconds from this center. The velocity range of each spectrum is 0–1000 km s^{-1} and the brightness temperature range is -0.08 – $+0.16$ K.

only linear baselines. The antenna temperature (T_A^*) was corrected for telescope and atmospheric losses by the calibration procedure. We adopt the main beam scale $T_{mb} = T_A^* / \eta_{mb}$ for the antenna temperature, with $\eta_{mb} = 0.56$ for the CO(1-0) line. The integrated emission is given by: $I(\text{CO}) = \int T_{mb} dv$ K km s^{-1} .

2.3. The $H\alpha$ data

The $H\alpha$ image (Fig.3) was obtained by J.R. Roy and P. Martin with the 1.6m of Observatoire du Mont Mégantic employing a $f/8 \rightarrow f/3.5$ focal reducer, in May 1988. The exposure time was 5 times 2000 sec with a 6577/10 filter. The FWHM of the filter ($\sim 10\text{\AA} = 457 \text{ km s}^{-1}$) covers the whole velocity range of the HI data. NGC 4548 was observed with a RCA chip 360×512 pixels (scale of 1.1 arcsec/pix).

The images were reduced using the software package IRAF following the procedures described in Belley & Roy (1992) and in Martin & Roy (1992). Two sources of uncertainties relevant to the present analysis must be pointed out. First the accuracy of monochromatic flux measurement in the inner regions depends on how well the relatively bright stellar continuum in the central regions is subtracted; the final result is somewhat uncertain because the continuum filter used is about 400\AA to the red side of $H\alpha$. A first order subtraction is usually done using relative scaling of the flux of several stars in the field. The result-

ing monochromatic image is that where the base level $H\alpha$ flux in interarm regions (apart the presence of interarm HII regions) shows net zero flux in the monochromatic image; this is achieved after careful steps of trial and error. Previous to this, subtraction of the sky background has been done. This brings up the second source of uncertainties, which is the accuracy of the flat fielding procedure. This is quite critical because it affects the measurements of mean $H\alpha$ surface brightness in the faint outer regions. Uncertainties arise because of the restricted field and of the difficulties of eliminating large-scale variations of the background illumination to better than 2-3 % in monochromatic imagery done with our focal reducer. To circumvent this, we eliminated the regions of weak surface brightness by applying conservatively a high cut-off to the data. We kept only *individual* pixels which had number of counts (in ADU) greater than the rms value above the background in the annulus were the total number of counts was not longer seen to increase with increasing galactocentric distance.

Finally, the images were calibrated using the aperture spectrophotometry done by McCall (1982).

2.4. The optical data

A CCD B image of NGC 4548 (Fig.2) was obtained at the NOAO 0.9 m telescope at Kitt Peak², Arizona, in June 1995. We used a 2048x2048 T2KA detector ($2 e^-/\text{ADUs}$) in the f/13.5 configuration, which gives a field of view of $13.1' \times 13.1'$ with a pixel size of $0.4''$. The galaxy was observed through the Kitt Peak B Harris filter in a 15 min exposure during non photometric conditions. The image was reduced using standard procedures, including bias correction, dome flat fielding and cosmic ray removal. The seeing was $\sim 2''$.

3. Results

The complete HI data cube is shown in Fig.2. The flux added over all channels with a cutoff of 2σ is shown in Fig.3. The total flux calculated using a cutoff of 2σ is $S_{\text{HI}} = 9.4 \text{ Jy km s}^{-1}$. This corresponds to a total HI mass of $M_{\text{HI}} = 6.4 \times 10^8 M_{\odot}$ with a distance $D = 17 \text{ Mpc}$ for the Virgo cluster³. This is in good agreement with the value given by Cayatte et al. (1990) using a larger beam size of $55'' \times 55''$.

The HI emission is distributed within an almost complete ring. The maximum of emission is located in the south-east. The emission profile along the minor axis is quite symmetrical, whereas the one along the major axis

² Kitt Peak national Observatory, National Optical Astronomical Observatories, which are operated by the Association of Universities for Research in Astronomy, Inc. (AURA), under cooperative agreement with the National Science Foundation.

³ We assume $H_0 = 75 \text{ km s}^{-1} \text{ Mpc}^{-1}$.

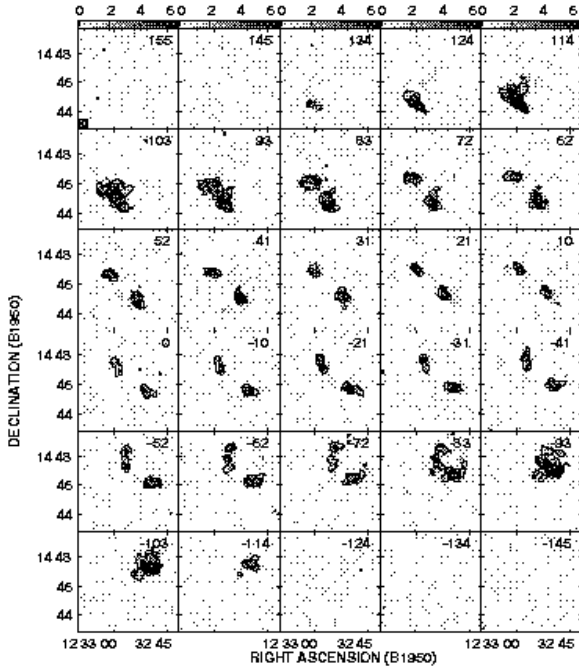


Fig. 2. The HI channel maps. The heliocentric velocity relative to the reference velocity is indicated in km s^{-1} in the upper right of each channel. The contour lines are 1.3, 2.6, 3.9, 5.2, and 6.5 mJy/beam.

is strongly asymmetrical. In fact the south-eastern emission maximum has no counterpart in the north-west. The near Infrared image of Boselli et al. (1997b Fig.3b) shows clearly the bar and the two spiral arms in the north-west and south-east. As for the HI emission, there is more NIR emission coming from the southern part of the galaxy. In addition, the outer limits of the NIR emission coincide well with the one of the HI emission. Thus, the intensity of the HI emission follows the gravitational potential traced by the NIR image. In the galaxy's centre the HI emission drops by an order of magnitude leading to an in east-west direction elongated hole. It is also worth noticing that the inner edge of the emission ring extends more inwards in the north than in the south.

In order to compare the galaxy's gas content to its stellar population, we show the HI emission together with an optical B image in Fig.3. One clearly recognizes the bar which ends at the inner edge of the HI ring. It is also visible that both the low contrast spiral arms are traced by the HI emission. The local HI emission maximum in the extended southern arm is associated with the young stellar population traced by the spiral arm. The outer edge of the atomic gas ring follows exactly the shape of the stellar

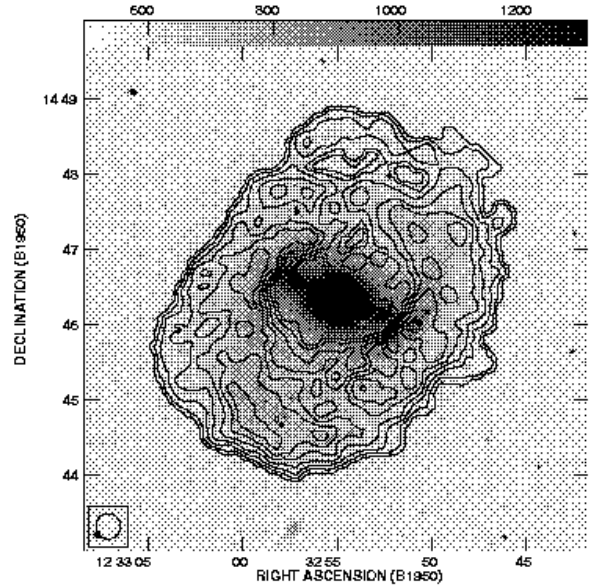


Fig. 3. The optical B image together with the HI contour map of NGC 4548. The contour levels correspond to 0.82, 3.24, 6.48, 9.73, 12.97, 16.21, $19.45 \times 10^{20} \text{ cm}^{-2}$. The beam is shown in the lower left corner. In order to distinguish maxima and minima we refer to Fig.5.

disc. A dust lane is seen in absorption near the centre in the south-west. If one accepts the idea that it is not located in the inner disc, this indicates that the eastern side is the near side of the galaxy.

As expected for an anemic spiral galaxy the $\text{H}\alpha$ line map shows very few HII regions. In Fig.4 we show this map together with the HI emission map. The most luminous HII regions are located along the beginning of the spiral arms at the end of the bar. There the interaction between the bar and the outer gas favours star formation.

The CO emission was observed in a $120'' \times 120''$ region centered on the galaxy. These data together with the HI map are shown in Fig.5. As expected, the bar appears clearly in the CO emission. We can also observe the points where the local CO emission maxima join the HI emission maxima at the ends of the bar.

Honma et al. 1995 demonstrated that the gas phase transition between HI and H_2 occurs within a small radial distance. The fraction of H_2 to the total gas column density (molecular fraction) increases very rapidly inwards within this boundary region. In order to study this effect for NGC 4548, the deprojected distance for each CO point-

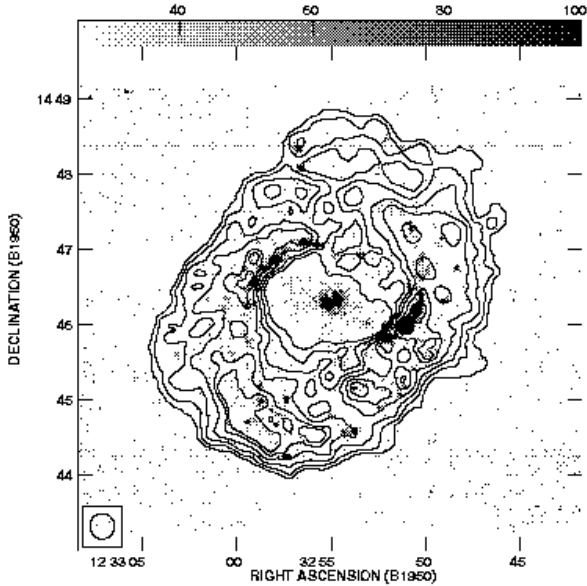


Fig. 4. Contour plot of the HI emission map together with the H α image. The contour levels correspond to column densities of 3.44, 6.89, 10.33, 13.78, 17.22, 19.29 $\times 10^{20}$ K km s $^{-1}$ cm $^{-2}$. The HI beam is shown in the lower left corner.

ing to the galaxy centre was calculated with the help of the position angle and the inclination (see next section). As the HI and CO data have similar beam sizes it is possible to compare the column densities at a given position. The fraction of column densities $x = N_{H_2}/(N_{H_2} + N_{HI})$ for each CO pointing is plotted as a function of the deprojected distance (Fig.6). We assumed CO conversion factor of $X = 1.0 \pm 0.1 10^{20}$ cm $^{-2}$ (K km s $^{-1}$) $^{-1}$ as derived by the EGRET gamma-ray observations (Digel et al. 1996) for the solar neighbourhood. However, in the Perseus arm at 3-4 kpc from the Sun $X = 2.5 \pm 0.9 10^{20}$ cm $^{-2}$ (K km s $^{-1}$) $^{-1}$ (Digel et al. 1996). For extragalactic sources there are only estimations ranging from $X \simeq 0.6 10^{20}$ cm $^{-2}$ (K km s $^{-1}$) $^{-1}$ for M51 (Guélin et al. 1995) to $X \simeq 10 10^{20}$ cm $^{-2}$ (K km s $^{-1}$) $^{-1}$ for the SMC (Lequeux et al. 1994). In general it seems that X does not differ by a large factor in spiral galaxies with a luminosity similar to the Galaxy (Boselli et al. 1997a). Therefore, we have adopted a factor 3 for the uncertainties in the determination of X . The error bars in Fig.6 represent these uncertainties. As there is no HI detection in the centre $x = 1$ there. The molecular fraction tends to decrease with radius up to $\sim 40''$ which corresponds approximately to the radial extent of the bar.

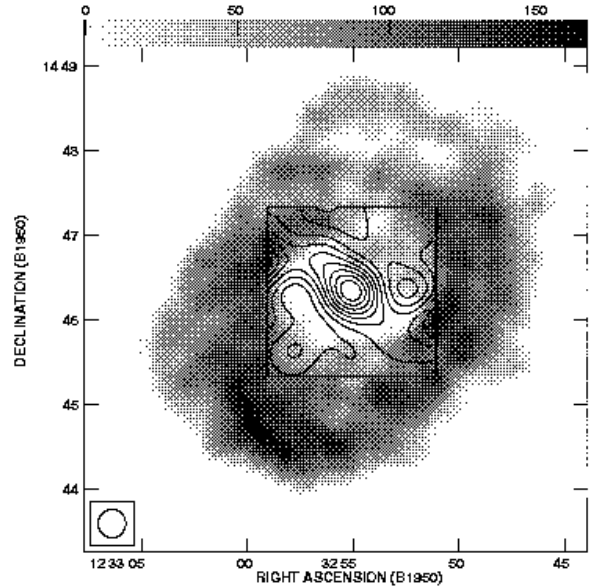


Fig. 5. The HI emission map from Fig.3 together with CO emission contour map. The maximum level is 10.87 K km s $^{-1}$. The contour levels are in steps of 1.09 K km s $^{-1}$. The HI beam is shown in the lower left corner.

There the predominantly atomic gas appears to be transformed into molecules due to the compression caused by the bar. Further out the molecular fraction does not show a further decline. This means that we observe a sharp transition between molecular and atomic gas at about 30'' and a constant molecular gas fraction $x = 0.27 \pm 0.09$ (assuming $X = 10^{20}$ cm $^{-2}$ (K km s $^{-1}$) $^{-1}$) further out.

4. Kinematics

4.1. The rotation curve

The HI emission map together with the contours of the intensity weighted mean velocity field is plotted in Fig.7. The overall velocity field is in good agreement with an almost unperturbed rotation around the galaxy centre. Nevertheless, we can see a distortion in the south-east caused by the spiral arm which is very prominent in HI there. A minor distortion can also be seen in the north-west, where the other spiral arm is located. There are first hints that the northern part of the galaxy has a somewhat peculiar velocity field which does not fit the rest.

The position angle and the inclination were determined using a tilted ring model (see Begeman 1987). We have

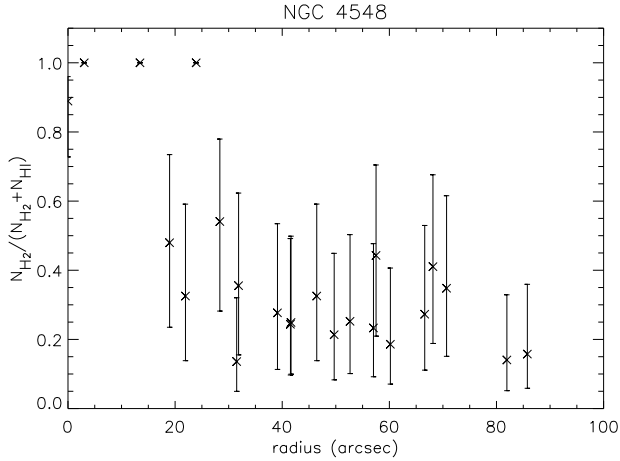


Fig. 6. The molecular fraction at each CO pointing. Its values as a function of the deprojected distance to the galaxy centre are shown. The error bars correspond to conversion factors of $X/3$ and $X \times 3$.

Table 2. Col. (1) Author. Col. (2): Position angle of the major axis. Col. (3): inclination angle. Col. (4): systemic velocity in km s^{-1} . Col. (5): maximum rotation velocity in km s^{-1} .

author	position angle	inclination	v_{sys}	v_{max}
Vollmer	$136 \pm 0.5^\circ$	$25 \pm 6^\circ$	477 ± 1	254 ± 47
Guhathakurta	135°	42°	504	200
Rubin	136°	38°	475	200

used the optical central position (Table 1) and a systemic velocity of 475 km s^{-1} (Rubin et al. 1999) as initial values. We averaged first the approaching and receding side of the galaxy up to a radius of $115''$ excluding points within a sector of $\pm 30^\circ$ around the minor axis. The derived dynamical centre is the optical one $\pm 3''$. The results for the other parameters are given in Table 2.

The systemic velocity is in excellent agreement with the value of Rubin et al. (1999) and agrees well with the value given by Cayatte et al. (1990), whereas the value given by Guhathakurta et al. (1988) differs by $\sim 5\%$. The position angle is in excellent agreement with Rubin et al. (1999) and Guhathakurta et al. (1988). The main difference between the two authors and us is the value of the inclination angle. Our value is about $10\text{-}15^\circ$ lower than the ones previously derived. This is due to the complex structure of the rotation curve which we will discuss now. In a second step we fixed the dynamical centre and the systemic velocity of the tilted ring model and fitted the approaching and receding side separately. The resulting inclination angle increases for both sides with increasing radius. The rotation velocity stays constant in the south-eastern part of the galaxy. On the north-western side it

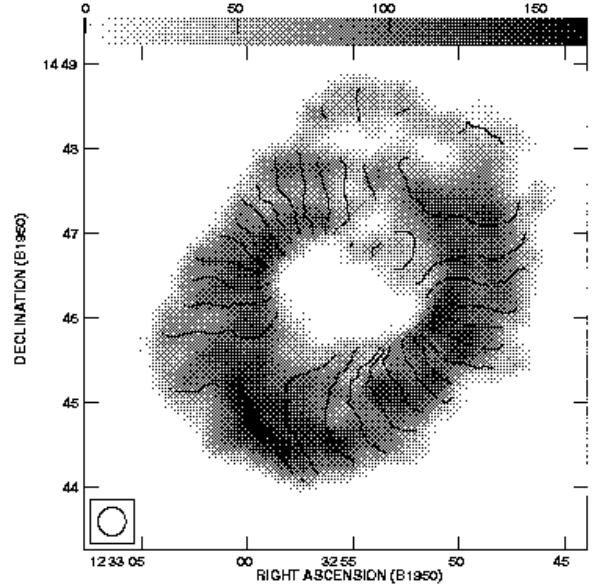


Fig. 7. The HI emission map together with the contours of the intensity weighted mean velocity field. The peak contour level is at 602 km s^{-1} in the south-east of the galaxy centre. The contour levels are in steps of 15 km s^{-1} northwards. The HI beam is shown in the lower left corner.

decreases up to $140''$ and then increases with increasing radius. In order to compare our rotation curve with the one of Rubin et al. (1999) we fixed the inclination angle at 27° for both data. This choice gives coherent rotation curves. Both rotation curves are shown in Fig. 8. It is best fitted by a constant rotation velocity of $\sim 250 \text{ km s}^{-1}$. For radii greater than $120''$ the rotation curves of the two sides diverge. The nearly constant slope in the rotation curve of the receding side in our data suggests that this is due to a rising inclination angle. In order to investigate on the change of the inclination we fixed the rotation velocity at 250 km s^{-1} . In this case the inclination angle has the same behaviour as the rotation curves in Fig. 8. It has the same value up to a radius of $\sim 110''$ and diverges for greater radii. The difference in the shape of the rotation curve with the one derived by Guhathakurta et al. (1988) is due to the fact that their data had twice the beam size and five times less sensitivity. The worse angular resolution caused major beam smearing effects and the low sensitivity permitted only to fit the rotation curve to a smaller part of the HI emission revealed by our observations. The consequence is that they derived a more steeply

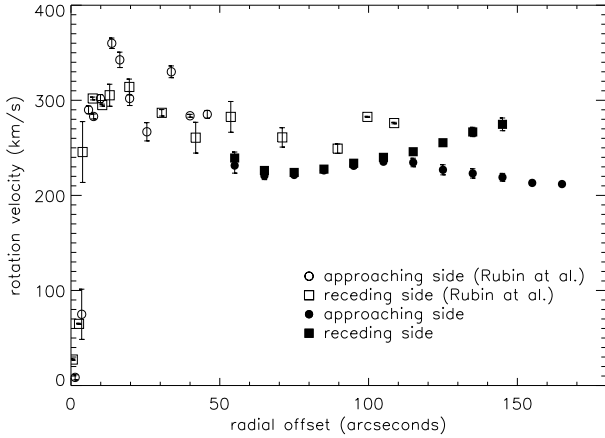


Fig. 8. The rotation curve of NGC 4548. The open boxes and circles are the Rubin et al. (1999) data. The filled boxes and circles represent our data. The bars indicate the errors on the measurements. If they are not visible, they do not extend further than the symbol size.

rising rotation curve with increasing radius for both sides. The divergence of the rotation curve for radii greater than $120''$ could be due to three extreme cases. (i) The rotation velocity is constant and the inclination angle decreases at the western side and increases for the eastern side. (ii) The inclination angle stays approximately constant for both sides. In this case the neutral gas is accelerated in the east and decelerated in the west. (iii) The inclination angle increases for both sides and the gas at the western side is decelerated. A tilted ring model where the rotation curves are fitted separately for each side using the same increasing inclination angle (Fig.9) gives residuals which are approximately 3 times less than those of the previous models. Therefore, this hypothesis seems to be the most probable.

4.2. A three dimensional method to visualize the HI data cube

In order to have a more detailed and complete view of the kinematics, it is necessary to look at the data cube as a whole in three dimensions to separate connected features more clearly⁴. All velocity channels seen in Fig.2 are piled up to give the cube. The cube's axes are right ascension, declination and heliocentric velocity. All points in the cube having intensities exceeding a chosen level become opaque, the rest being transparent. The surface created in this way is illuminated by light which is coming out of the observer's direction. Thus, brighter features are closer to the observer. This representation allows to analyse the whole cube from any possible point of view. The data cube visualized in this way with an intensity level

⁴ The visualizations are done with IDL (version 5.1).

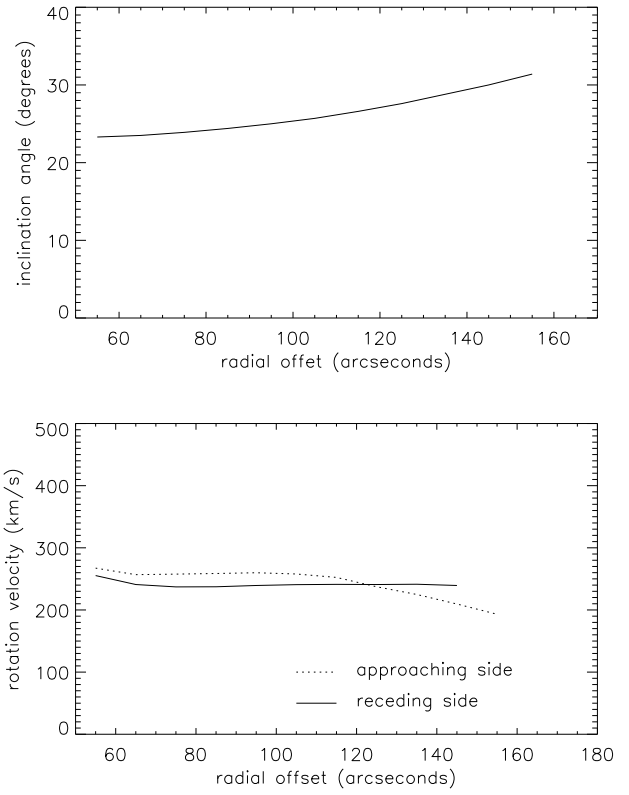


Fig. 9. Top: Inclination angle of both sides with respect to the radial offset for case (iii). Bottom: The resulting HI rotation curves for the approaching and receding side.

of 2 mJy/beam (5σ) is plotted in Fig.10. The z-axis is perpendicular to the image plane. It corresponds to Fig.3 with the important difference that this is a three dimensional representation where the third axis is perpendicular to the image plane. In order to examine the detached arm, we turn the cube $\sim 180^\circ$ around the heliocentric velocity axis. This can be seen in Fig.11. In this representation the constant rotation velocity translates into a ring in the three dimensional restricted phase space (α , δ , heliocentric velocity). The most interesting things happen in the north, where the detached arm described above can be clearly distinguished.

It has the shape of a filament 'warped' around the constant velocity ring in the restricted phase space. The emission blob at the top corresponds to the emission blob in Fig.10 which reaches into the central hole from the north-west. It is the emission nearest to the galaxy centre. The complexity of the rotation curve described above can be observed directly as a discontinuity of the three dimensional velocity field in the north.

4.3. Adding the CO pointings to the cube

The 23 points can be easily included into the data cube. Because of the sparseness of the CO detections it is not

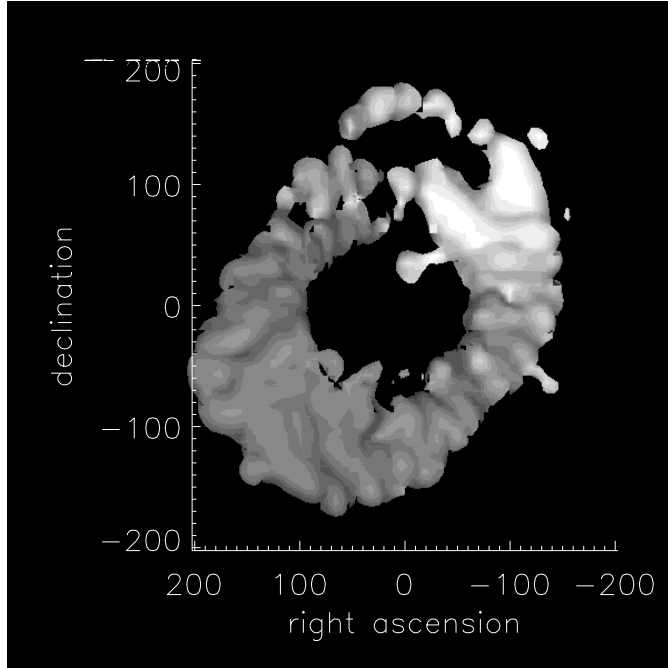


Fig. 10. Three dimensional visualization of the data cube with an intensity level of 2 mJy/beam. The brighter the structures are the nearer they are to the observer.

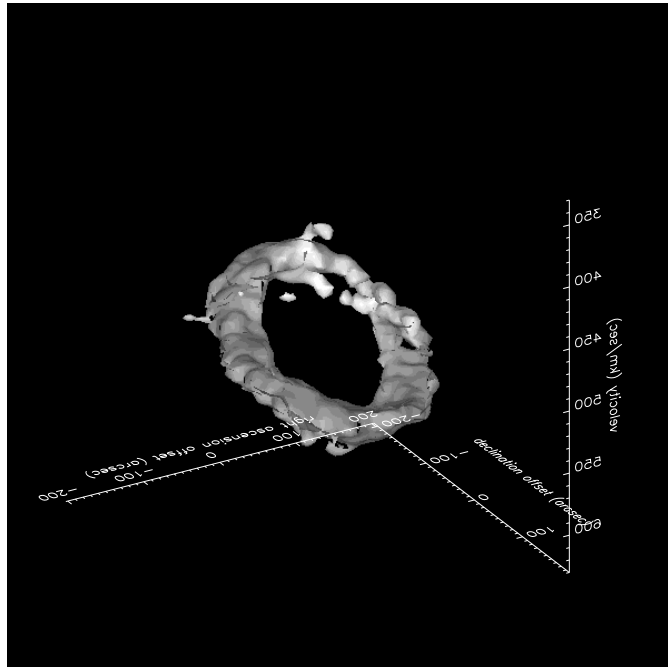


Fig. 11. The same cube as in Fig.10 but rotated by $\sim 180^\circ$ around the heliocentric velocity axis.

possible to apply an interpolation in order to have a continuous velocity field. As the HI cube has a quasi continuous nature whereas we have only 23 discrete points in CO, we have to adjust the CO intensity and smooth it in the following way. In order to have the best view of

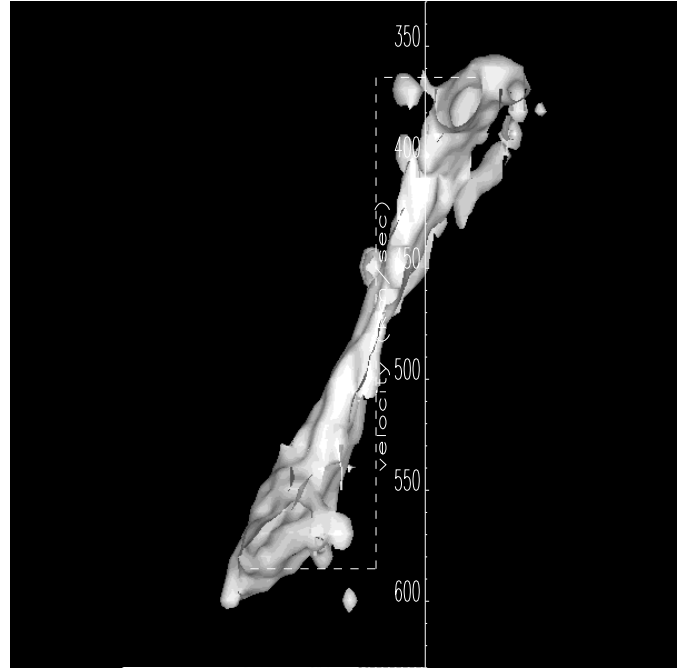


Fig. 12. The constant velocity rotation ring seen edge-on. The $\alpha - \delta$ plane is perpendicular to the image plane, the velocity axis is seen vertically. The case of ideal constant velocity rotation is shown by the broken line.

the ensemble we decided to normalize the maximum CO intensity to that of the HI intensity. Then each CO data point is smoothed with a Gaussian filter with a FWHM of $20''$. The CO pointings are now spheres in the restricted phase space whose radii are comparable to the beam size which are easily visible in contrast to the surrounding HI features. It should be stressed that the aim of this procedure is to compare HI and CO velocities, disregarding any flux conservation.

Now we have to investigate if the CO points which lie inside the contours have the same velocities as their HI counterpart. Furthermore, making a single cube of both data will permit us to see if there is a smooth junction in the restricted phase space between the spatially inner CO point and the outer HI emission structure. Fig.12 shows the ring of constant velocity rotation edge-on. The detached arm is located in the north. The $\alpha - \delta$ plane is perpendicular to the image plane, the heliocentric velocity axis is seen vertically. With the help of this image two conclusions can be drawn. (i) The CO points indicate that the rotation with approximately constant velocity extends further into the centre as the CO points fit into the ideal constant velocity field which is sketched by the dashed line. Especially the HI blob nearest to the galaxy centre described above has a CO pointing nearby which fits perfectly into the constant velocity rotation scenario. (ii) The CO points match nicely into the HI data cube. No major discrepancies are detected except a point which is located in the bar. But as this gas is expected to be highly perturbed, this is not sur-

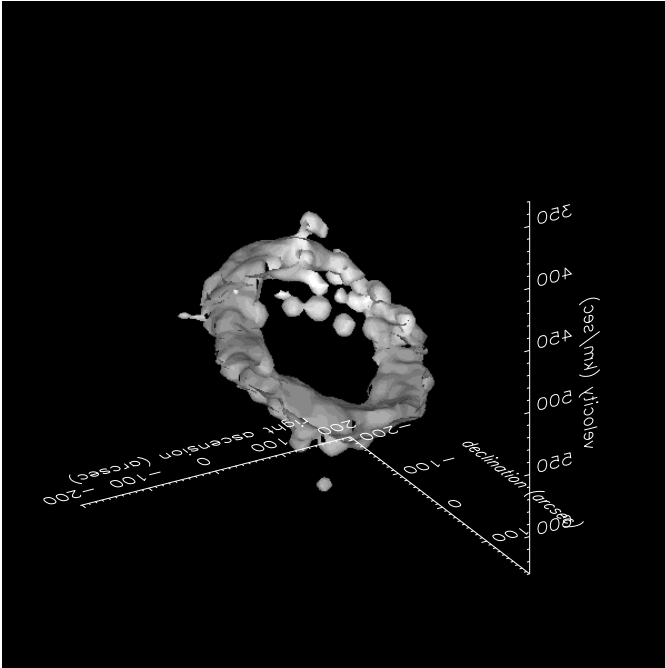


Fig. 13. The same view as in Fig.11 but with the CO points included. The spheres within the constant velocity rotation ring are the pointings which lie on the bar. The CO points located within the HI ring are nicely embedded in the HI emission.

prising. In this figure one can easily recognize the greater velocities as expected for a constant velocity rotation in the east and the lower velocities compared to a constant velocity rotation in the west. Finally, in order to show the nice smooth junction between both data, Fig.13 shows the same view as in Fig.11 but including the CO points. Here one can see the CO spheres embedded nicely in the HI structures.

4.4. First order modeling

As the velocity field from $50''$ up to $100''$ (projected radius) is known, it is possible to make a simple model and compare it directly with the cube. We have distributed 10000 points in two dimensions between $50''$ and an outer deprojected radius r_{out} . A constant azimuthal velocity of 250 km s^{-1} was attributed to them. At the end a randomly chosen velocity vector with a length of up to 10 km s^{-1} (van der Kruit & Shostak 1982) and a randomly chosen direction in three dimensions was added to the velocity of each point. With this model velocity field a cube similar to the one discussed above can be constructed. As the given field is one single realization of the model and we are interested in the general case, we smooth the model cube with a second order Gaussian filter. This corresponds - through hydrostatic equilibrium - to a certain thickness of the HI disk. We then subtracted the model cube from the data cube. This procedure gives us the emission structure

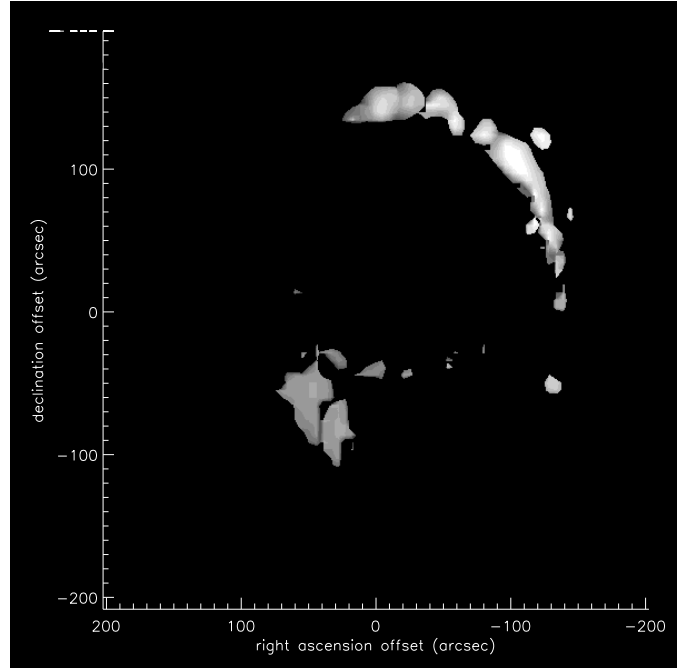


Fig. 14. Residual of the subtraction of the model cube from the HI data cube.

which can not be explained by a constant velocity rotation field ranging between $50''$ (deprojected radius) and r_{out} . The outer radius is fixed by the following condition. We begin with a small number, say $100''$ and increase it as long as there is a residual in the south east of the image (Fig.3). This procedure gives us a radius of $r_{\text{out}}=135''$. The final residual is shown in Fig.14. As a result, the complete northern detached arm appears very clearly. So this part of the galaxy is not located within the given radius in the disk plane. In addition, parts of the spiral structure in the south-east whose velocity field differs from the constant velocity rotation are visible.

If we extend the outer deprojected radius in the model to $r_{\text{out}}=170''$, even the northern arm can be recovered by the model. The modeling applied allows us to determine easily which model points correspond to emission points in the cube above the given level. The deprojected distribution of sites of HI is therefore accessible. It is shown in Fig.15 as dark lines. The grey lines correspond to an intensity level in the HI cube which is half of the one previously used. They correspond to the noise level in the cube. The reconstructed low intensity extended emission velocity field shows a well defined straight ridge from the eastern to the northern edge. In addition, in the north the galaxy's outer HI emission extends further to the north than expected assuming a constant outer galactic radius. In the reconstruction using the higher intensity level the northern detached arm clearly appears. The detached blob which can be seen in Fig.10 at $\alpha \sim -120''$, $\delta \sim 120''$ is recovered by the model too. It is quite remarkable that the upper part of the northern arm has already here a well

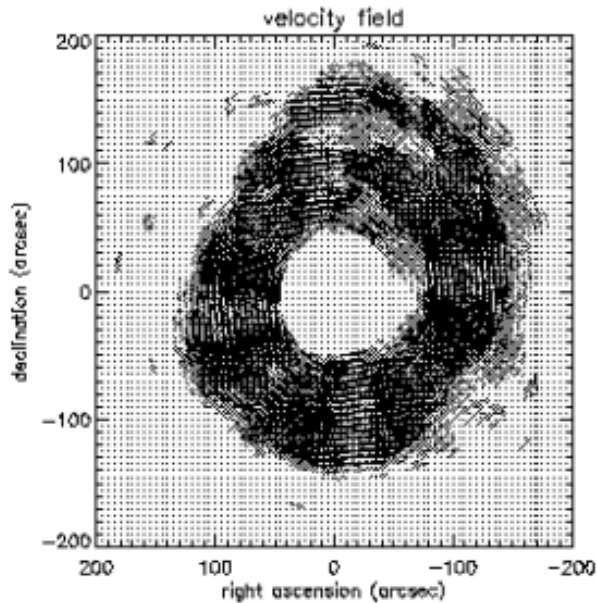


Fig. 15. The reconstructed sites of HI emission. Dark: only velocity vectors of model points corresponding to emission in the data cube above the given level are plotted. Grey: the intensity level in the HI cube is lowered by a factor 2.

defined vertical edge.

The next stage in modeling is to include a simple warp. Placing all model points exceeding $r=135''$ in a plane which is inclined by 15° with respect to the galaxy's plane appeared to be a good fit to the data. In this case the northern arm is located in projection behind the galaxy's plane. The distance between the northern arm and the galaxy centre is thus bigger in this case than in the one assumed above. Applying the same procedure as before, gives similar results. The fact that we have only emission at one side of the galaxy together with the smallness of the tilt angle does not permit any distinction between the two cases. Therefore the modeling of a increasing inclination angle does not give very different results for the reconstructed HI emission distribution.

It should be stressed here that the aim of the modelization is not to reproduce the exact velocity field of the HI data but to show general effects. The conclusion which can be drawn is that there is an asymmetrical structure in the deprojected disk which can be fitted by a much increased outer radius of the galaxy or by material which is located in tilted plane with respect to the galaxy's plane. This confirms the results of the tilted ring model. Furthermore, we can see a well defined north-eastern ridge in the reconstructed velocity field for the low intensity extended HI emission in both models.

5. Discussion

We will now discuss the possibilities to explain the complex structure of the velocity field in the restricted phase space.

- If the galaxy's outer deprojected radius is $\sim 170''$, the whole northern arm with the detached blob at $\alpha \sim -120''$ $\delta \sim 120''$ is located within the plane of the disk. This represents the simplest case and is shown in Fig.15. In this case the neutral gas in the eastern part of the galaxy is accelerated and the gas in the western part is decelerated.
- The northern arm could be located beyond the disk plane in which the galaxy is located. The rotation velocity is still constant. In this case the inclination angle diverges for radii greater than $120''$.
- The rotation velocity field is distorted, but the gas moves in the plane of the galaxy whose inclination angle increases with increasing radius. This means that the material in the eastern part is strongly decelerated (Fig.9).
- The velocity field is distorted and the gas is not located in the galaxy plane. This is the most complicated case and can only be verified if a dynamical model is applied.

The fitting of the tilted ring model already gives an idea which possibility is the most probable one. The three dimensional representation completes the analysis giving additional hints which possibility is preferable. The two methods are thus complementary. As Fig.11 shows a clear discontinuity of the velocity field in the north, we think that an increasing inclination angle for both sides is most likely. This confirms the conclusion derived with the tilted ring model. In addition, Fig.15 shows a 'perturbed' HI emission distribution and therefore atomic gas mass distribution (the detached northern arm and the north-eastern ridge). This suggests that the same mechanism which produces the ridge might be responsible for the complexity of the rotation curve and especially the perturbation of the velocity field in the north. Thus, the constant velocity assumption is not the whole story for the northern detached arm.

The near-IR H band image of NGC 4548 (Boselli et al. 1997b) which traces fairly well the gravitational potential does not show a significant asymmetry in the north which could be responsible for the disturbed velocity field. Therefore, an external force is necessary to cause and/or to maintain the north-eastern ridge and the northern perturbation. NGC 4548 is located at a projected distance of 2.4° of the cluster centre (M87). If we suppose that the deprojected distance is not significantly higher, the galaxy is moving in a high temperature ($T \sim 10^7$ K) and low density ($\rho \sim 10^{-4} \text{cm}^{-3}$, Böhringer et al. 1994) gas at a speed of $v \sim 1000 \text{ km s}^{-1}$. Cayatte et al. (1994) have shown that assuming these conditions the ram pressure

of the hot intra-cluster medium can exceed the restoring force of the galaxy's gravitational potential. So it is very probable that this external ram pressure force can explain the observed perturbation in the atomic gas content.

Nevertheless, we can not entirely exclude that this is a case of a warp not induced by ram pressure. HI warps are a common feature of spiral galaxies (see e.g. Bosma 1981, Briggs 1990, Bottema 1995). In their sample of 1700 galaxies Richter & Sancisi (1994) found that 50% of the galaxies show asymmetries, non-circularities, or lopsidedness in the HI distribution. Reshetnikov & Combes (1998) showed that in their sample of 540 galaxies half of them have optical warps. The majority of HI warps can be described by a tilted ring model, where the position angle and the inclination change with radius for the whole galaxy. Compared to these warps, the distortion in the velocity field of NGC 4548 shows one important difference: the divergence of the inclination angle and/or the rotation velocity.

Other possibilities for the explanation of the distorted velocity field are a perturbation of the halo, a recent accretion of a dwarf galaxy, or a perturbation of the gravitational field by one of the two nearby dwarf galaxies or by the gravitational potential of the cluster. In all these cases the perturbation must have happened very recently ($t \sim 10^8$ yr) to show the observed asymmetry.

Instead, if we accept that the atomic gas content is removed when the galaxy passes near the center (Cayatte et al. 1994) this galaxy may have already passed the cluster once as it is highly HI deficient. So we observe either

- the fading effects of the ram pressure stripping if the galaxy is moving away from the cluster centre,
- the increasing effects of a new stripping process in the opposite case,
- the effects of a halo perturbation,
- the influence of the accretion of a dwarf galaxy
- a mixture of these effects.

Both perturbations due to gravitational interaction do not explain the north-eastern ridge neither the divergence of the inclination angle / rotation velocity in a natural way. On the other hand, ram pressure acts more efficiently on clouds of small column density. Therefore it would be only natural to observe its consequences on gas with a small column density (which corresponds to a region of low gravitational potential), i.e. the detached northern arm and the north-eastern ridge. This confirms the conclusion drawn above, i.e. that the galaxy's inclination angle rises for both sides and that the gas in the north-east is decelerated. In addition, NGC 4548 has a radial velocity of about -800 km s^{-1} with respect to the cluster centre (M87). If the eastern side is in front of the western one as the absorption feature suggests, the galaxy's motion is directed to the north-east. The pressure due to the intra-cluster medium decelerates the neutral gas of low column density. This deceleration is observed for the detached northern arm (Fig.12).

6. Conclusion

We have shown a high sensitivity HI data cube of NGC 4548 together with 23 pointings in CO(1-0), an H α line map, and an optical B image. The HI emission shows a ring-like structure which is symmetric along the minor axis and asymmetric along the major axis. Particularly, there is a distorted low intensity arm in the north. The comparison of this data with an optical B image showed that the HI emission follows the spiral arms. The detached northern arm however, has no detectable counterpart in the B image. The dust lanes appearing in the south-west places this side behind the eastern part of the galaxy.

The H α line emission shows several bright HII regions at the ends of the bar.

The CO(1-0) data covers $120'' \times 120''$ centered on the galaxy. The bar appears clearly and joins the HI emission at the end of the bar. The molecular fraction stays constant for galactic radii greater than $40''$ and rises rapidly between $20''$ and $40''$.

We have determined the position angle and the inclination and have fitted a rotation curve to the atomic gas data. The velocity field can be described either by a constant velocity rotation of ~ 250 km s^{-1} and a diverging inclination angle for the outer parts or by a constant inclination angle and a diverging rotation velocity for the outer parts or by something in between. The difference in the shape of the rotation curve with the one derived by Guhartakurta et al. (1988) can be explained by the better angular resolution and the much better sensitivity of our data.

We choose a three dimensional visualization of the data to show the detailed velocity field. In three dimensions the constant velocity rotation corresponds to a ring in the restricted phase space (α , δ , heliocentric velocity). The detached northern arm is clearly visible and it appeared that it is distorted in velocity too. The inclusion of the CO data into the atomic gas cube gives insight into the kinematics of the central region and fits nicely with the data of Rubin et al. (1999).

A simple model of a disk with constant rotation velocity is fitted to the data. In the reconstructed emission map we observe an asymmetry in the north. We list the different possibilities for the causes of the distorted velocity field and discuss them in detail.

We conclude that the ram pressure stripping scenario is entirely consistent with all observational constraints and might be the dominating effect. If this is the case there might be the possibility to have a pile-up of the intracluster medium in front of the galaxy in the direction of its motion. X-ray observations with XMM detecting this pile-up may thus confirm our conclusions. Furthermore, we will investigate further on this topic using detailed dynamical models of this scenario. The galaxy's velocity with respect to the cluster centre (M87), the orientation of the disk and the detailed shape of the perturbations will enormously constrain the model parameters. Dynamical models are

therefore a precious tool to investigate on the observed perturbations.

Acknowledgements. We would particularly like to thank J.R. Roy and P. Martin for making their H α data available. We thank V. Rubin for making available her data prior to publication, J. Braine for fruitful discussions, and the referee for useful advices. We thank also the VLA staff for their kind support during the observations.

BV is supported by a TMR Programme of the European Community (Marie Curie Research Training Grant).

References

- Barnes J.E., Hernquist, L., 1996, ApJ, 471, 115
 Belley, J., Roy, J.-R., 1992, ApJS, 87, 61
 Begeman K., 1987, Ph.D. thesis, University of Groningen
 Bica M.D., Giovanelli R., 1987, ApJ, 321, 645
 Binney J., Jiang I.-G., Dutta S.N., 1998, MNRAS, 297, 1237
 Binney J., 1992, ARA&A, 30, 51
 Böhringer H., Briel U.G., Schwarz R.A. et al., 1994, Nature, 368, 828
 Bothun G., Schommer R.A., Sullivan W.T.III, 1982, AJ, 87, 731
 Boselli A., Gavazzi G., Lequeux J. et al., 1997a, A&A, 327, 522
 Boselli A., Tuffs R.J., Gavazzi G. et al., 1997b, A&A, 121, 507
 Bosma A., 1978, PhD Thesis, Groningen Univ.
 Bosma A., 1981, AJ, 86, 1791
 Bottema R., 1995, A&A, 295, 605
 Briggs F., 1990, ApJ, 352, 15
 Casoli F., Boissé P., Combes F., Dupraz C., 1991, A&A, 249, 359
 Cayatte V., van Gorkom J.H., Balkowski C., Kotanyi C., 1990, AJ, 100, 604
 Cayatte V., Kotanyi C., Balkowski C., van Gorkom J.H., 1994, AJ, 107, 1003
 Chamaraux P., Balkowski C., Gérard E., 1980, A&A, 83, 38
 Combes F., Dupraz C., Casoli F., Pagani L., 1988, A&A, 203, L9
 Combes F., 1997, in IAU Symp. 186, Galaxy interactions at Low and High Redshift, Eds: D.B. Sanders & J. Barnes, p. 25
 Digel S.W., Grenier I.A., Heithausen A., Hunter S.D., Thaddeus P., 1996, ApJ, 463, 609
 de Vaucouleurs G., de Vaucouleurs A., and Corvin H.G. Jr., 1976, Second Reference Catalogue of Bright Galaxies (University of Texas, Austin)
 Forveille T., Guilloteau D., Lucas R., 1990, IRAM internal report (CLASS)
 Gavazzi G., 1987, ApJ, 320, 96
 Gavazzi G., 1989, ApJ, 346, 59
 Gavazzi G., Boselli A., Kennicutt R., 1991, AJ, 101, 1207
 Gavazzi G., Catinella B., Carrasco L., Boselli A., Contursi A., 1998, AJ, 115, 1745
 Giovanelli R., Haynes M.P., 1985, ApJ, 292, 404
 Guélin M., Zylka R., Mezger P.G., Haslam C.G.T., Kreysa E., 1995, A&A, 298, L29
 Guhathakurta P., van Gorkom J.H., Kotanyi C.G., Balkowski C., 1988, AJ, 96, 851
 Gunn J.E., Gott J.R., 1972, ApJ, 176, 1
 Honma M., Sofue Y., Arimoto N., 1995, A&A 304, 1
 Jiang I.-G., Binney J., 1999, MNRAS, 303, L7
 Kenney J.D., Young J.S., 1986, ApJL, 301, L13
 Lequeux J., Le Bourlot J., Pineau des Forêts G. et al., 1994, A&A, 292, 371
 Lynden-Bell D., 1965, MNRAS, 129, 299
 Martin, P., Roy, J.-R., 1992, ApJ, 397, 463
 McCall M.L., 1982, Ph.D. thesis, University of Texas
 Moore B., Katz N., Lake G., Dressler A., Oemler A., 1996, Nature, 379, 613
 Napier P.J., Thompson A.R., Ekers R.D., 1983, Proc. IEEE 71, 1295
 Nelson R.W., Tremaine S., 1995, MNRAS, 275, 897
 Olson K.M., Kwan J., 1990, ApJ, 349, 480
 Quinn T., Binney J.J., 1992, MNRAS, 255, 729
 Reshetnikov V., Combes F., 1998, A&A, 337, 9
 Richter O.-G., Sancisi R., 1994, A&A, 290, L9
 Rogstad D.H., Lockhart I.A., Wright M.C.H., 1974, ApJ, 193, 309
 Rubin V., Waterman A.H., Kenney J.P.D., 1999, AJ, in press
 Ryden B.S., Gunn J.E., 1987, ApJ, 318, 15
 Ryden B.S., 1988, ApJ, 329, 589
 Sancisi R., 1976, A&A, 53, 159
 Sparke L., 1984, ApJ, 280, 117
 Sparke L., Casertano S., 1988, MNRAS, 234, 873
 Valluri M., 1993 ApJ, 408, 57
 van den Bergh S., 1976, ApJ, 206, 883
 van der Kruit P.C., Shostak G.S., 1982, A&A, 105 351
 van Gorkom J.H., Kotanyi C.G., 1985, in Proceedings of the Workshop on the Virgo Cluster, edited by O.G. Richter and B. Bingelli (ESO Garching), p. 61
 Warmels R.H., 1988, A&AS, 72, 19